École Polytechnique Fédérale de Lausanne

Investigating Beam-Induced Electron Emission from Thin Wires in Proton Beams and Bias Voltage Influence

REPORT

Jerome Touguet

18th February 2025

Abstract

The emission of electrons induced by beam interaction with thin targets is a critical phenomenon used to measure various properties of particle beams. Among these mechanisms, thermionic emission plays a significant role in shaping electron behavior and influencing measurement accuracy. A common technique to suppress this emission involves applying a bias voltage to the wire, recapturing low-energy electrons. This study investigates these mechanisms under the influence of bias voltage and their impact on the measurement process for high-brightness proton beams of the HIPA accelerator. Through experiments and simulations, the study aims to better understand the emission spectra, the suppression of thermionic emission, and the effects of beam fields on electron dynamics.

Contents

1 PSI and HIPA presentation **3**
- 1.1 PSI in brief . . . 3
- 1.2 The proton accelerator facility HIPA . . . 4
  - 1.2.1 The main components of HIPA . . . 4
  - 1.2.2 The main applications of HIPA . . . 5

2 Beam Instrumentation **6**
- 2.1 Transverse beam profile monitor . . . 6
- 2.2 Beam transverse profile measurements: wire scanner . . . 6
- 2.3 PSI's Main Ring Cyclotron Radial Probe (RRL) . . . 7
- 2.4 Modular profile and position monitors in UCN(cross wire) . . . 8
- 2.5 Main beam properties . . . 9

3 Interaction between the wire and the beam **11**
- 3.1 The energy deposition . . . 11
- 3.2 Wire signal: Secondary, thermionic and δ electrons . . . 12
  - 3.2.1 δ electron emission . . . 12
  - 3.2.2 Secondary electron emission . . . 13
  - 3.2.3 Thermionic emission . . . 15

4 Recapture of low energy electron in presence of bias voltage **18**
- 4.1 Application of the Bias voltage . . . 18
- 4.2 Simulation/Numerical computation . . . 22
- 4.3 Limits on bias voltage . . . 23

5 Impact of the beam in the recapture **25**
- 5.1 Beam impact on the applied voltage to recapture secondary electrons:experiment . . . 25

6 Thermionic emission **32**

7 Conclusion and Perspectives **36**

Chapter 1

PSI and HIPA presentation

1.1 PSI in brief

The Paul Scherrer Institute (PSI), established in 1960, is Switzerland's largest research center for natural and engineering sciences, located in Villigen. It operates under the Swiss Federal Institute of Technology (ETH Zurich) and plays a pivotal role in advancing scientific knowledge and innovation.[1]

Figure 1.1
Aerial view of the PSI facilities (Photo: Paul Scherrer Institute)

PSI's research is organized into three main areas:

- **Materials Science:** PSI focuses on the study of materials at the atomic level using neutron and X-ray scattering techniques. This research aids in understanding material properties, leading to innovations in electronics, energy storage, and nanotechnology.
- **Energy Research:** The institute is actively involved in the development of sustainable energy solutions, including research into nuclear fusion and renewable energy sources. PSI's work on advanced materials and processes contributes to improving energy efficiency and reducing carbon footprints.

- **Health Research:** PSI is a leader in medical physics, particularly in the fields of particle therapy and imaging techniques. The institute develops innovative methods for cancer treatment and advanced imaging modalities, enhancing diagnostic capabilities and treatment effectiveness.

To support its research, PSI hosts several world-class facilities:

- **High-Intensity Proton Accelerator (HIPA):** A unique proton accelerator facility which will be described more in detail in the next Section.
- **Proton therapy system (Proscan):** fed by COMET (Compact Medical Cyclotron) cyclotron, which can treat deep-seated tumors with two gantries of different types and eyes tumours with Optis2 beamline.
- **Swiss Light Source (SLS):** A fourth generation synchrotron light source that generates high-intensity X-rays, enabling researchers to conduct experiments across various scientific fields, including biology, chemistry, and materials science.
- **Swiss Free Electron Laser:** This facility produces intense, ultrafast X-ray flashes that allow researchers to study the properties of matter in real time, opening new avenues in fundamental research and materials science.

1.2 THE PROTON ACCELERATOR FACILITY HIPA

The High Intensity Proton Accelerator Facility (HIPA) at PSI is a world-leading accelerator providing a 1.4 MW continous proton beam, with three steps of acceleration, driving cutting-edge research in materials science, particle physics, and neutron science with its record-setting beam current and a suite of advanced experimental facilities[2].

1.2.1 THE MAIN COMPONENTS OF HIPA

- **The proton source**
  The first step in proton production is the proton source, where hydrogen gas is heated with microwaves to strip electrons from the atoms, leaving only the atomic nuclei composed of a single proton. The source used at PSI is based on the Electron Cyclotron Resonance (ECR) phenomenon, where electrons in the source chamber move in circular orbits, colliding with many atoms. This type of source enables the generation of high-intensity ion beams. The protons exiting the source have a kinetic energy of 60 keV.
- **The Cockroft and Walton DC acceleration**
  The Cockcroft-Walton pre-accelerator is the first stage of the HIPA Facility[3]. It generates a continuous proton beam by accelerating protons from the ion source, increasing their kinetic energy from 60 keV to 870 keV using a constant potential difference of 810,000 volts. The system consists of a cascade high-voltage generator, placed inside a large Faraday cage, and connected to a high-voltage platform.
- **Injector 2**
  Injector 2 is a cyclotron that accelerates protons to 72 MeV, with an extraction capacity of up to 2.7 mA of proton current. The proton beam transitions from a DC beam to CW mode, utilizing three high-frequency resonators operating at 50 MHz[4]. These are supplemented by two additional resonators at 150 MHz, originally designed as 'flat-top resonators,' ensuring a stable and continuous output for downstream applications.

- **Main Ring Cyclotron**
  The Ring cyclotron is designed to extract a fixed beam energy of 590 MeV[5]. The 72 MeV proton beam from Injector 2 is injected at a radius of 2.048 m, accelerated in approximately 180 revolutions, and extracted at full energy at a radius of 4.448 m. Its design supports high beam intensities, with a structure that includes four high-power RF cavities operating at 50 MHz, and a flat-top cavity operating at 150 MHz. With a maximum beam current of 2.4 mA and a beam power of 1.4 MW, HIPA is the world's most powerful continuous beam particle accelerator.

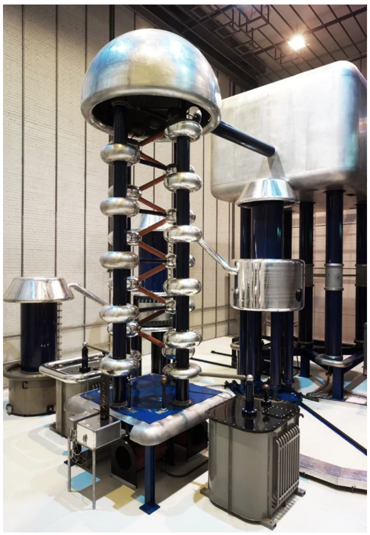

(A) Cockcroft and Walton DC accelerator (Photo: Paul Scherrer Institute)

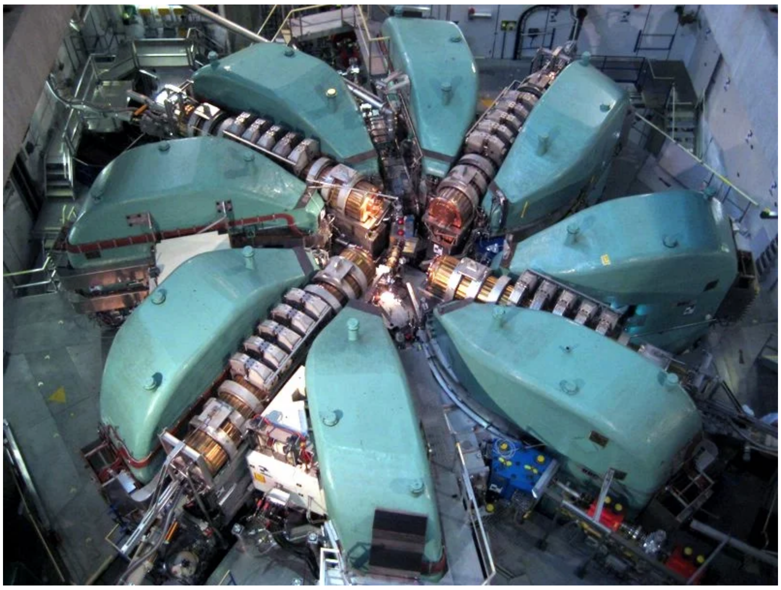

(B) Main Ring (Photo Paul Scherrer Institute)

FIGURE 1.2

1.2.2 THE MAIN APPLICATIONS OF HIPA

The 590 MeV proton beam is used for different application in research.

- **Muon source (SμS)**: The SμS muon source[6] generates muons by directing fast protons onto carbon graphite targets, producing pions, which then decay into muons and neutrinos. This process provides polarized, low-energy muons ideal for studying magnetic properties in solids, with the ability to decelerate them for experiments on thin films or surfaces.
- **Spallation neutron source (SINQ)**: SINQ is producing a high neutron flux of about 10^{14} n/cm^2/s[7]. Neutrons are generated through proton-driven spallation, where protons from the HIPA accelerator strike a target material and knocks the neutrons out of the lead nuclei. It offers thermal neutrons, making it ideal for materials research as new semiconductors and neutron radiography and tomography.
- **An ultracold neutron source (UCN)**: Ultracold neutrons are produced through spallation in a lead target[8][9], followed by moderation and conversion in specialized materials as solid deuterium at 5K. These neutrons, with their extremely low kinetic energy typically below 1 neV, are ideal for high-precision experiments, as they can be trapped and studied in great detail. The search for the neutron electric dipole moment (nEDM) was the first measurement using the UCN source.

CHAPTER 2

BEAM INSTRUMENTATION

2.1 TRANSVERSE BEAM PROFILE MONITOR

A transverse beam profile monitor is an essential diagnostic tool used in particle accelerators to assess and optimize the beam characteristics, particularly its spatial distribution across the transverse plane. This monitor typically measures parameters such as beam size, shape, and intensity distribution, providing information for ensuring efficient acceleration and delivery of particle beams.

The transverse beam profile is measured using various techniques, including wire scanners, SEM-grids, scintillation screens, ionization profile monitor or rest gas fluorescence monitors. Scintillation screens, for example, utilize materials that emit light when struck by particles. A camera or photodetector captures the emitted light, allowing for a two-dimensional profile reconstruction of the beam. This method is useful in low-intensity beam environments, where beam does not provoke damage to the material.

2.2 BEAM TRANSVERSE PROFILE MEASUREMENTS: WIRE SCANNER

A wire scanner is a widely used diagnostic tool in particle accelerators for measuring the transverse profile of a particle beam[10]. The device consists of a thin wire that is precisely traversed through the beam's path. In a wire scanner, one measurement method involves detecting scattered particles outside the vacuum chamber. When beam particles have energies above 150 MeV, they interact with the wire through multiple scattering and nuclear reactions, producing scattered particles with large angles that are detected by sensors around the chamber. This scattered signal reveals details about the beam profile.
An alternative method uses secondary electron emission current for detection. As the wire passes through the beam, it intercepts particles, generating an induced electrical current proportional to the beam's intensity at each position. By recording this current along the wire's path, the scanner builds a one-dimensional density profile of the beam.The moving support can be either linear or rotational. A linear setup moves the wire straight across the beam for a simple, high-resolution profile. A rotational setup pivots the wire in an arc, ideal for tighter spaces and capturing multi-angle profiles. Linear systems offer precision and simplicity, while rotational systems can scan faster (up to 20 m.s^{-1}), reducing wire heating and allowing ofr faster scans.
At low beam energies, wire scanners directly interact with the beam, causing significant scattering or stopping of particles. For higher energy beams, the disturbance is minimal, but beam loss can occur, which can be problematic in high-intensity machines.
Wires made of tungsten, molybdenum, and carbon fibers are currently the preferred materials for thin

targets in high-power beams due to their excellent combination of thermal, mechanical, and electrical properties[11]. Other materials used include beryllium, silicon carbide, tantalum, quartz, carbon nanotubes and titanium.
The targets are considered thin when their thickness is less than of the order of 100 μm and can even go

Material	Density [g.cm^{-3}]	Melting Temperature [K]	Atomic Number (Z)
Tungsten	19.3	3695	74
Molybdenum	10.3	2896	42
Carbon fiber	2.1	3915 (sublimation)	6
Carbon nanotube	0.2–1.8	3915 (sublimation)	6

TABLE 2.1
Properties of thin target materials[12]. For carbon fiber and carbon nanotube, the sublimation temperature is shown instead of the melting temperature, as carbon melts only under very high pressures.

down to submicrometer levels.The thickness of the target is important in the conception of a wire scanner. Indeed, the small thickness of these targets results in a higher surface-to-volume ratio, which lowers temperature due to surface-dominated cooling, reduced energy deposition as some electrons are ejected during particle interactions, and minimized beam perturbations, making wire scanners in high-energy proton machines nearly non-intercepting devices. The limits in thickness results by the way they are handled and mounted and the signal we can observe.

2.3 PSI'S MAIN RING CYCLOTRON RADIAL PROBE (RRL)

For the PSI's Main Ring Cyclotron, the transverse beam profile is measured using the Long Radial Probe (RRL)[13]. This wire scanner scans all orbits along the cyclotron radius, ranging from approximately 2.048 m (inner radius) to 4.480 m (outer radius) and with beam from 72 MeV at injection to 590 MeV at the last orbit. The RRL consists of three wires: a vertical one and two tilted at $\pm 45°$ angles. These

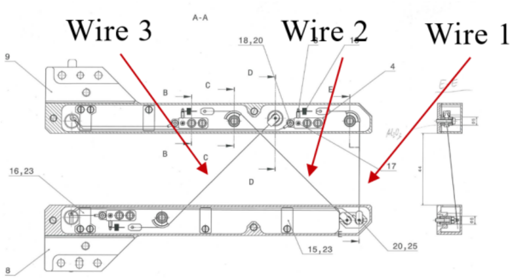

FIGURE 2.1
Schema of the three wires mounted on two trolleys moving synchronously (Courtesy of Martin Rohrer/Paul Scherrer Institute)

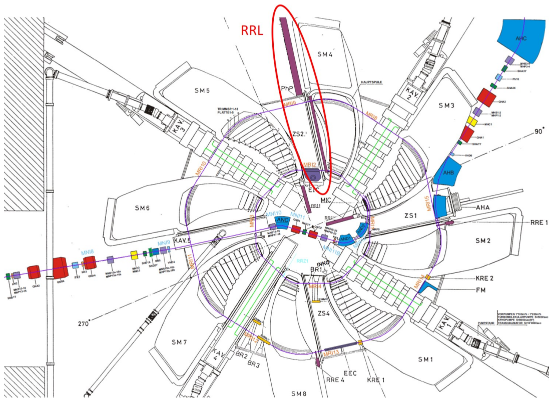

FIGURE 2.2
Top view of the Main Ring Cyclotron with RRL position (Technical drawing: Paul Scherrer Institute)

wires measure the horizontal and diagonal profiles, and through a few manipulations, the vertical profile can also be derived. The wires are made of carbon fibers, with a diameter of 34 μm, and are mounted on trolleys that move synchronously, powered by the same stepper motor and identical drive mechanisms. The trolley speed is 29.7 mm/s and the duration of a measurement is about 3 min.

The entire structure of the RRL is designed to be placed in or removed from the cyclotron without disrupting the vacuum. The wire signals are read out by a MESON module, which includes logarithmic current amplifiers and digitizes the signal at a rate of 2 kHz. The electronics are located outside the cyclotron bunker, with the cables spanning approximately 86 meters. A main consideration for the wire scanner in RRL is its proximity with RF cavities which involves a heat of the wire and possible damage on it. Each scan generates around 160,000 data points per wire and per direction, with the three wires

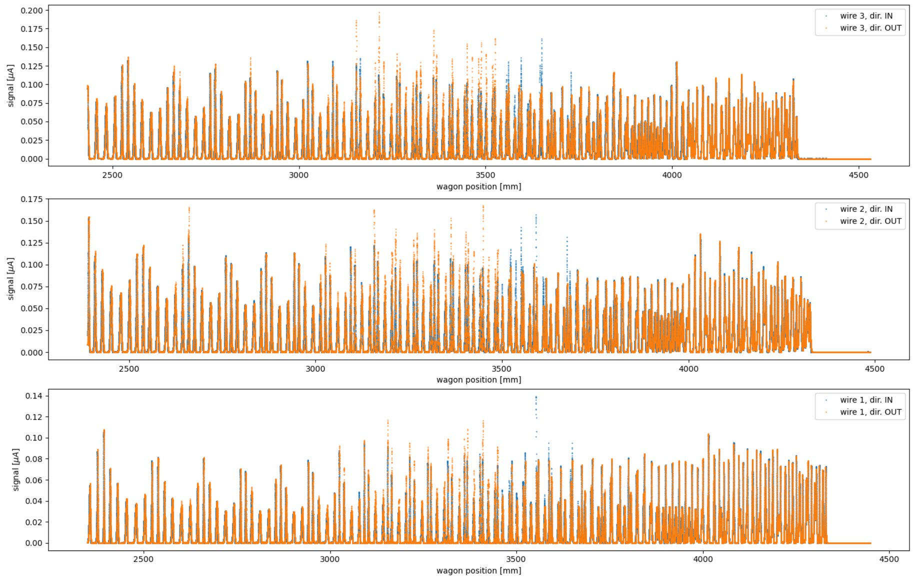

FIGURE 2.3
Scan IN and OUT of the full profile for 100 µA beam current, with the 186 orbits, for the three wires.

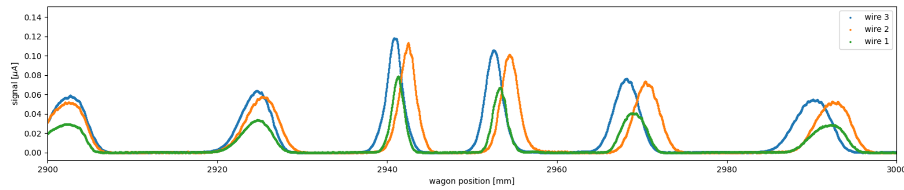

FIGURE 2.4
Scan IN of the profile for 100 µA beam current between radius of 2.9m and 3.0m, with the 186 orbits, for the three wires.

representing different signal strengths. During each scan, the trolleys move from the outermost position toward the machine center (scan IN) and then back (scan OUT). The tilted wires provide larger signals due to their longer contact time with the beam, resulting from their 45° angle, which increases the contact time by a factor of $\sqrt{2}$, as we observe in the zoomed profile measurement in Figure 2.4.

2.4 MODULAR PROFILE AND POSITION MONITORS IN UCN(CROSS WIRE)

The wire scanner prototype is located in a beamline towards the UCN[14]. The beam to UCN can be delivered in two modes: continuously as a split beam (a few µA) or as a full deflected beam of 2 mA for 8 seconds, with a 400-second repetition cycle. The beam profile at the location of the considered scanner is particularly challenging due to the narrow vertical width, which results in the highest thermal load on the

wire monitor compared to other beamlines, such as those at 590 MeV.
The scanner consists of both horizontally and vertically moving wires, with the horizontal wires (MBPT1)

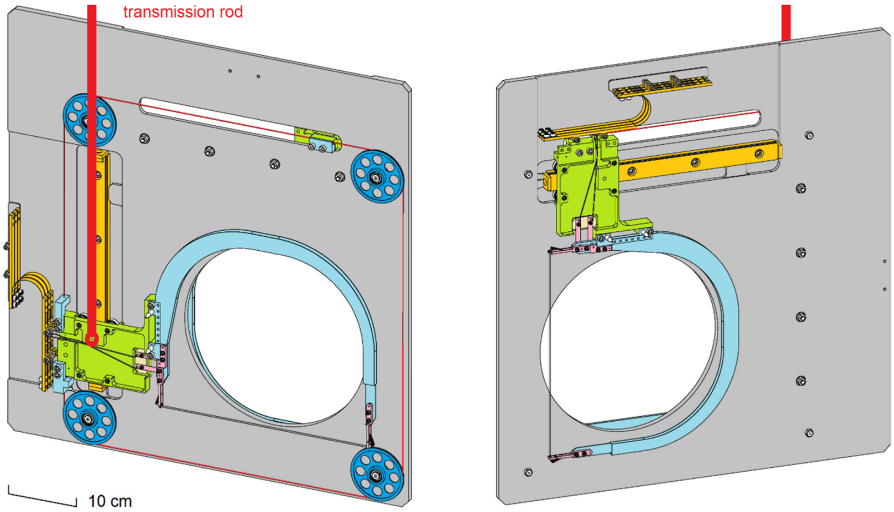

FIGURE 2.5
Front and rear side of Profile monitor module (Courtesy of Rudolf Dölling)

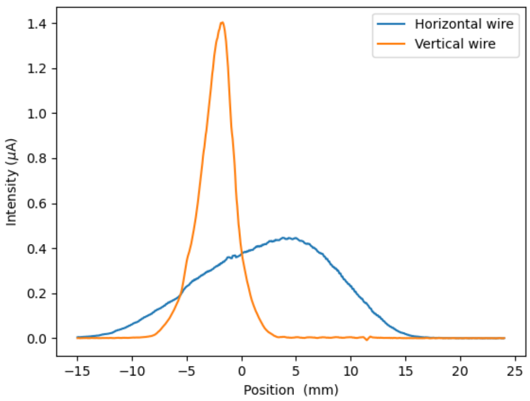

FIGURE 2.6
Profile measurement on vertical and horizontal wires of MBPT12 scanner for 2 mA beam.

experiencing a higher thermal load than the vertical wires (MBPT2). During each scan, the horizontal and vertical wires move synchronously through the beam, both forward and backward, "meeting" at the beam axis twice. The wire speed of the prototype is slower than typical wire scanners, operating at only 0.06 m/s. This slower speed is a result of the maximum step rate of 2 kHz, which is dictated by the MESON modules driving the stepper motor and reading the signal currents from the wires. To address the challenges posed by the low wire speed and high heating, they have chosen for the horizontal wire a 40 μm diameter carbon nanotube wire and for the vertical wire a 25 μm diameter molybdenum wire.

2.5 MAIN BEAM PROPERTIES

For the profile measurement and further simulations, beam properties are key parameters to know, and especially in the Main Ring where there is energy change for each of the 186 turns.

- **Energy gain per turn**:To calculate the kinetic energy of a beam at a specific orbit in the Main Ring, we consider that the beam gains approximately 0.84 MeV of energy in each resonator. The energy at orbit n, denoted as E_n, can be determined using the following equation:

$$E_n = E_0 + (n-1) \cdot 4 \cdot 0.84 \tag{2.1}$$

where E_0 represents the injection energy, which is 72 MeV for the Main Ring Cyclotron. This formula is an approximation because the electric field inside the cavity has a sinusoidal shape, causing the acceleration to be less efficient at the initial and final orbits. Additionally, the fifth cavity, which operates at 150 MHz and is designed to increase the longitudinal acceptance of the machine, also affects the accelerating field. The particles undergo acceleration through roughly 186 orbits to reach an energy of 590 MeV.

- **Beam intensity**:In HIPA, beam intensity can be modulated from fractions of μA to 2.2 mA now and are pushing for even higher current. In RRL, thermionic emission seems to appear in the signal for beam intensity of around 1 mA.

- **Beam shape**:The beam shape refers to the way in which the particles are distributed in the bunch. In most cases, the bunches have a Gaussian shape, and in particular, the transverse distribution of the particles follows a-two dimensions Gaussian distribution, centered at (x_0, y_0):

$$P(x,y) = \frac{1}{2\pi \cdot \sigma_x \cdot \sigma_y} \exp\left(-\frac{(x-x_0)^2}{2 \cdot \sigma_x^2} - \frac{(y-y_0)^2}{2 \cdot \sigma_y^2}\right) \tag{2.2}$$

where σ_x and σ_y are the transverse sizes of the beam. It is important to note that in cyclotrons, the transverse beam shape can deviate from a Gaussian distribution. However, for this case, we assume the beam to be Gaussian. Moreover, for the longitudinal plane, in HIPA, the shape is a little bit different because the cavity at 150 MHz was built in such way to increase longitudinal acceptance and becoming flatter in the center that a Gaussian beam. we need also to consider the repetition rate of 50 MHz. Nevertheless, for simulations, we will consider also a Gaussian distribution:

$$P(x,y,t) = \frac{1}{2\pi \cdot \sigma_x \cdot \sigma_y \cdot \sigma_t} \exp\left(-\frac{(x-x_0)^2}{2 \cdot \sigma_x^2} - \frac{(y-y_0)^2}{2 \cdot \sigma_y^2} - \frac{(t-t_0)^2}{2 \cdot \sigma_t^2}\right) \tag{2.3}$$

- **Beam size**: The longitudinal size of the beam is nearly constant for different energy and intensity. The standard deviation was measured, in the lab frame, to be: $\sigma_t = 200$ ps[15].
In the transverse plane, the beam size is dependent of the orbit and the beam intensity. However, measurements in HIPA show an empirical relation between beam size and beam current following a power law. The exponent in the relation was founded to be close to 1/3:

$$\sigma(I) \approx \sigma(I_0) \left(\frac{I}{I_0}\right)^{1/3} \tag{2.4}$$

This empirical law enables the estimation of the beam size where there is thermionic emission, from beam sizes at low beam intensities, without thermionic emission.

Chapter 3

Interaction between the wire and the beam

3.1 The energy deposition

When a charged particle crosses through matter, it mainly interacts with the electrons, losing its energy. This energy loss depends on the type of particle, the beam energy, and the target material. A practical way to describe the amount of lost energy is using the concept of *stopping power*, which is the energy lost per unit length of the particle's track in the material, normalized to material density. For heavy particles, like protons, it is calculated using the Bethe-Bloch formula :

$$-\left\langle \frac{dE}{dx} \right\rangle = K \frac{z^2 Z}{A} \frac{1}{\beta^2} \left[\frac{1}{2} \ln \left(\frac{2 m_e c^2 \beta^2 \gamma^2 W_{\text{max}}}{I^2} \right) - \beta^2 - \frac{\delta(\beta\gamma)}{2} \right], \tag{3.1}$$

where:

- z is the charge of the incident particle,
- Z is the atomic number of the medium,
- A is the atomic mass of the medium in g/mol,
- I is the mean excitation energy of the medium in eV,
- $\delta(\beta\gamma)$ is the density correction,
- β is the relativistic velocity ($\beta = v/c$),
- γ is the Lorentz factor ($\gamma = 1/\sqrt{1-\beta^2}$),
- $m_e = 511\,\text{keV}/c^2$ is the electron mass,
- $K = 4\pi N_A r_e^2 m_e c^2 = 0.307\,\text{MeV cm}^2\text{mol}^{-1}$ (where $N_A = 6.022 \times 10^{23}\,\text{mol}^{-1}$ is Avogadro's number and $r_e = 2.8\,\text{fm}$ is the classical electron radius),
- $W_{\text{max}} = \frac{2 m_e c^2 \beta^2 \gamma^2}{1 + 2\gamma \frac{m_e}{M} + \left(\frac{m_e}{M}\right)^2}$ eV is the maximum energy transfer in a single collision (where M is the mass of the incident particle in eV/c^2).

Stopping power is normalized to material density and has units of [MeV cm^2 g^{-1}]. It differs from linear energy transfer (LET), which is not density-normalized and has units of [MeV cm^{-1}].

Usually, most of the energy lost by the particle is deposited in the material and can be considered as a heat influx. However, for very thin targets, such as in the case of carbon fiber, some of the electrons that gain high energy by interacting with the beam particles (so-called δ-electrons) escape, carrying away a significant fraction of the energy predicted by the Bethe-Bloch equation [16].

3.2 WIRE SIGNAL: SECONDARY, THERMIONIC AND δ ELECTRONS

In a wire scanner, the signal is generated by electrons emitted from the wire, which induce a current that is measured at the end of the system. The electron emission can arise from different processes—secondary emission, thermionic emission, or δ emission—each contributing differently to the wire signal in terms of magnitude and characteristics.[17]

3.2.1 δ ELECTRON EMISSION

δ-electrons are electrons that are kicked out of the target by an interaction with proton/ion. The energy transfer to the electrons in this binary interaction is relatively high and the electrons tend to leave the target with low interaction and scattering. These electrons carry away a significant fraction of energy (in the MeV range) and are referred to as delta rays—a term introduced by J.J. Thomson, the discoverer of the electron. In wire scanner systems, this emission is considered negligible compared to thermionic and secondary emissions but this statement will be discussed in this study. Moreover, the δ-emission depends on the material density, as higher densities produce more electrons. Additionally, the size of the target plays a dual role: a larger target increases the number of protons interacting with the material but makes it easier to stop the emitted electrons within the material.
Those electrons also affect the energy deposition in the Bethe-Bloch formula[17]:

$$-\left\langle \frac{dE}{dx} \right\rangle = \frac{4\pi}{m_e c^2} \cdot \frac{nz^2}{\beta^2} \cdot \left(\frac{e^2}{4\pi\epsilon_0}\right)^2 \cdot \left[\ln\left(\frac{2m_e c^2 \beta^2}{I \cdot (1-\beta^2)}\right) - \beta^2\right] \tag{3.2}$$

Moreover, we can also have the maximum energy transfer of a massive particle to an electron using this formula:

$$T_{\text{max}} = \frac{2m_e c^2 \beta^2 \gamma^2}{1 + \frac{2\gamma m_e}{M} + \left(\frac{m_e}{M}\right)^2} \tag{3.3}$$

For a 590 MeV proton beam, the maximum kinetic energy transfer to an electron is 1.68 MeV. Moreover, the maximum energy transfer, dependent on the electron's emission angle θ, follows binary encounter theory:

$$T_{\text{max}}(\theta) = \frac{2m_e c^2 \beta^2 \gamma^2}{1 + \frac{2\gamma m_e}{M} + \left(\frac{m_e}{M}\right)^2} \cdot cos^2(\theta) \tag{3.4}$$

A simulation was made using Geant4[18] and Monte-Carlo simulation to compute the electron energy and emission angle of electrons on a 33 μm diameter carbon wire of electrons ejected by primary protons and secondary particles at 590 MeV.
Indeed, we observe that the maximum kinetic energy transfer to the electron occurs in the forward direction, consistent with the predictions of the binary encounter theory. Additionally, we observe a broad distribution of electrons with energies lower than 200 keV. This low-energy electron population is primarily due to multiple scattering events and the production of tertiary electrons from delta electrons.
The emission angle of these secondary electrons is broad, and the average energy of the electrons in this band is around 92 keV. This phenomenon reflects the complex scattering process, where electrons are scattered multiple times in the target. Some tertiary electrons are generated by secondary electrons what further contributes to the broad distribution of energies and angles observed.

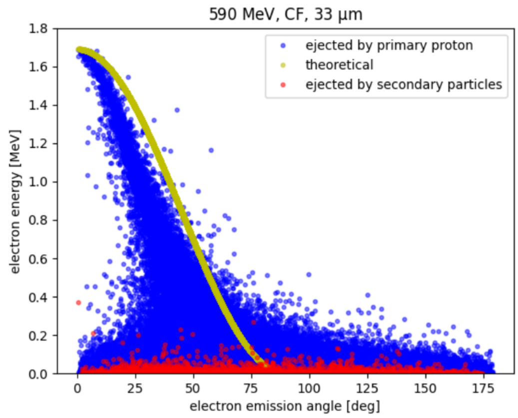

FIGURE 3.1
Simulation using Geant4 of electron energy and emission angle from a 590 MeV proton beam ejected by primary proton and secondary particles on a 33 μm carbon wire(Courtesy of Mariusz Sapinski)

3.2.2 SECONDARY ELECTRON EMISSION

By definition the particles emitted from the target, which were not present in the incoming beam are called secondary. In this sense also delta electrons are secondary. However, for historic reasons, the term „secondary electrons" is reserved for a specific type of low energy electrons emitted from the material.

Those secondary electrons arise from interactions between protons/ions and the material, transferring less energy per electron but affecting a larger group of electrons that undergo numerous collisions in the target material. In definitively, this process is better described as an interaction with an electron plasma, rather than as a series of binary collisions. Differences between δ and secondary electrons are illustrated in Figure 3.2.

Secondary electrons are described by the Sternglass model [19] and the emission is considered as a 3 step process:generation(ionization),diffusion,emission on the barrier.

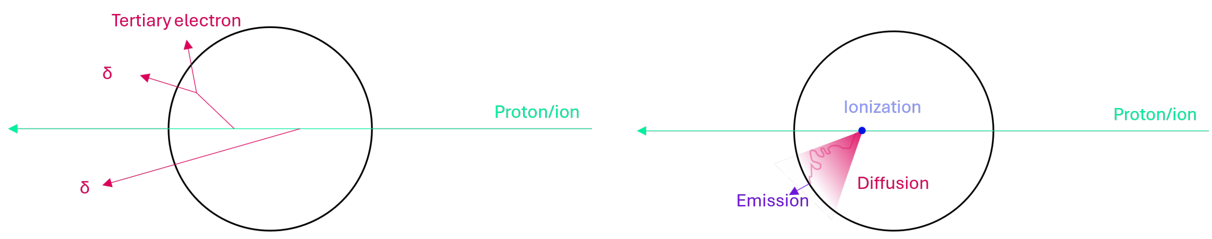

(A) δ electrons (B) Secondary electrons

FIGURE 3.2
Illustration of δ and secondary electron emission processes.

In this context, we use the Secondary Emission Yield (SEY) to quantify the average number of electrons emitted for each incoming particle. It can be calculated using the Sternglass formula [19]:

$$\mathrm{SEY} = 0.01 \cdot L_S \cdot \frac{dE}{dx} \cdot \rho \cdot \left(1 + \frac{1}{1 + 5.4 \times 10^{-6} \cdot \frac{E}{M}}\right) \tag{3.5}$$

In this equation:

- $\frac{dE}{dx}$ is the stopping power[20], measured in units of [MeV cm^2 g^{-1}],
- ρ denotes the density of the target material [g cm^{-3}],
- E is the kinetic energy of the incoming particle [eV],
- M is the mass of the incoming particle [eV],
- L_S is the characteristic distance between inealstic collisions in the material and it is defined as: $L_S = \frac{1}{3.68\times10^{-17}\cdot N_v\cdot Z^{1/3}}$ [cm], with N_v representing the atomic density (number of atoms per unit volume) and Z denoting the atomic number.

Upon impact of a projectile with a target, the secondary electron emission generates a charge Q_{SE}, which is described by the following expression [21]:

$$Q_{\text{SE}} = N_p \cdot \text{SEY}_p + N_p(1-\eta)\cdot \text{SEY}_p + N_p \cdot \text{BS}_p \cdot \text{SEY}_p, \tag{3.6}$$

where:N_p represents the number of protons in the projectile, SEY_p is the secondary emission yield for each proton, η is the fraction of protons that are stopped in the material, BS_p is the probability of protons being back-scattered.
In scenarios where the proton beam has zero probability of back-scattering and where none of the protons are stopped in the target, the secondary emission-induced charge simplifies to:

$$Q_{\text{SE}} = 2 \cdot \text{SEY}. \tag{3.7}$$

The charge Q_{SE} (generated per proton) can be multiplied by the total number of protons passing through the wire, thereby producing the wire signal. This signal is essential for reconstructing the transverse profile of the beam.
Nevertheless, the SEY is a theoretical value. The properties of the material surface can strongly affect the theoretical secondary electron production yield.
Moreover, the energy distribution of secondary emission electrons is challenging to describe accurately with theoretical models, as experimental results suggest that it varies significantly with both material characteristics and projectile properties.[22]

Thus, an approximate expression for electron bombardment is applied here[23]:

$$f_{\text{SE}}(E) = \frac{E - E_F - \phi}{(E - E_F)^4}, \tag{3.8}$$

where:

- E [eV] is the kinetic energy of the emitted electron,
- ϕ [eV] represents the material's work function,
- E_F [eV] is the Fermi energy level.

When the reference point for the Fermi level is taken just outside the material's surface, the work function ϕ becomes equal in magnitude but opposite in sign to the Fermi level E_F.

The energy distribution is challenging but, in general, secondary electrons have kinetic energies below a few tens of eV

3.2.3 THERMIONIC EMISSION

Unlike the previously described emission mechanisms, thermionic emission operates under entirely different principles and conditions. Indeed, thermionic emission is a mechanism of cooling where electrons are emitted from the wire when their thermal energy becomes sufficient to overcome the material's work function, $\phi(T)$ [eV]. This emission will contribute to the cooling due to the energy taken by the escaping electrons.[24]

Owen Richardson published a theory of thermionic emission in which the thermionic emission current density is given by the Richardson-Dushman equation[25]:

$$J_{\text{th}} = A_R \cdot T^2 \cdot \exp\left(-\frac{\phi}{k_B T}\right), \tag{3.9}$$

where:

- $A_R = \frac{4\pi m k_B^2 Q_e}{h^3} \approx 120.173\,\text{A cm}^{-2}\,\text{K}^{-2}$ is the Richardson constant,
- T is the absolute temperature,
- ϕ [eV] is the material's work function,
- k_B is the Boltzmann constant,
- m is the electron mass,
- Q_e is the elementary charge,
- h is Planck's constant.

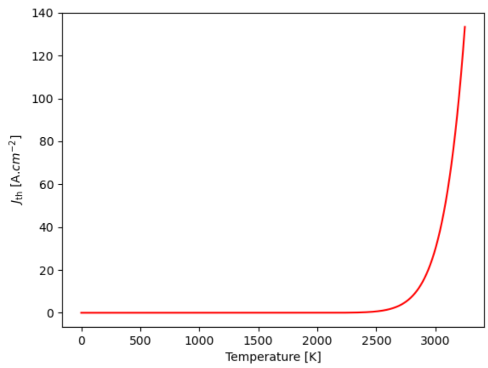

FIGURE 3.3
Thermionic current density as a function of temperature for a work function of 4.5 eV.

As seen in Figure 3.3, with low temperature, the thermionic current is very low due to this dependence on T^2 and in the exponential, but for higher temperature, it can be predominant over the other emission mechanisms. So, thermionic cooling is efficient for high temperature. The wire temperature depends on proton beam energy deposition and RF field, which generates heat. Nevertheless, unlike secondary and δ emission, thermionic emission can be considered detrimental to our measurement because it's not proportional to the number of charges passing by the wire and will deform the wire signal.

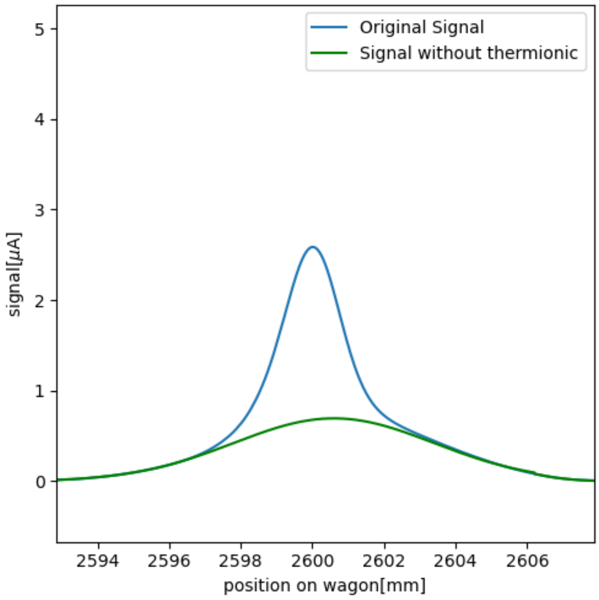

FIGURE 3.4
Comparison of signal profiles with and without thermionic emission correction in wire 2 at 1.6 mA corrected using Python

Indeed, in a profile measurement from RRL(Fig. 3.4), we observe that thermionic emission can be predominant compared to the signal and that we can lose the shape of the profile.
Thermionic emission occurs under extreme conditions characterized by high beam intensity and brightness, which is indeed the situation at HIPA. Moreover, in the context of HIPA profile measurement, the wire doesn't have the time to cool down between proton beam bunches, and so thermionic electrons are emitted continuously.
The energy distribution of thermionic electrons is given by [26]:

$$f_T(E) = (E - \phi) \frac{1}{1 + \exp\left(\frac{E-\phi}{k_B \cdot T}\right)} \cdot H(E - \phi), \tag{3.10}$$

where:

- $f_T(E)$ is the energy distribution of thermionic electrons,
- ϕ is the work function,
- k_B is the Boltzmann constant,
- T is the absolute temperature,
- $H(x)$ is the Heaviside step function.

We observe in Figure 3.5, that the majority of thermionic emission occurs at energies below 1 eV, while secondary electrons exhibit a peak energy at 2-3 eV, and with 50% of electrons with energy higher than

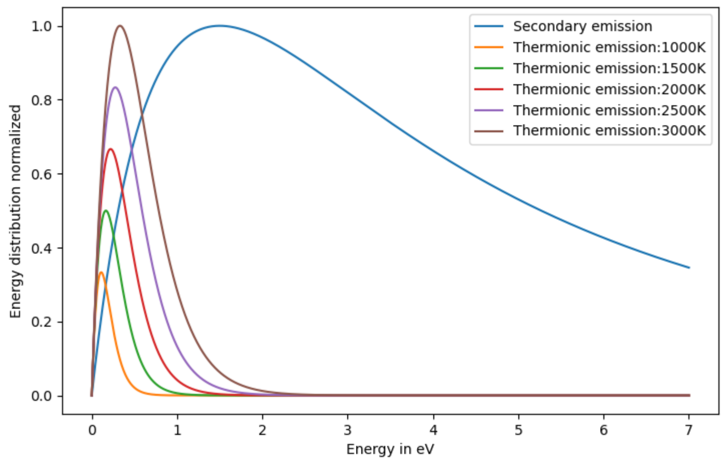

FIGURE 3.5
Energy distributions of thermionic and secondary emissions for a work function and Fermi energy of 4.5 eV at varying temperature

4.5 eV. This distinction highlights the differences in emission characteristics between thermionic and secondary electrons. This distinction in the emission spectrum is leveraged by applying a bias to the wire, allowing for the recapture of thermionic electrons. Nevertheless, in a previous study, we have observed that even with high bias, we still observe a distortion of the profile which was interpreted as a result of not complete elimination of thermionic emission [27].

CHAPTER 4

RECAPTURE OF LOW ENERGY ELECTRON IN PRESENCE OF BIAS VOLTAGE

4.1 APPLICATION OF THE BIAS VOLTAGE

To mitigate thermionic emission, wire scanners typically apply a bias voltage to the wire. This bias voltage helps recapture low-energy electrons, which is beneficial for isolating secondary electrons since they generally have higher kinetic energy compared to thermionic emission.
Nevertheless, this bias voltage also impacts the secondary electrons because part of it has the same energy. To observe this impact, we have done a measurement where we measured the wire current of the beam at a given beam intensity for different voltages in the absence of thermionic emission.
In the UCN setup, the wires were connected to a Libera current-meter, offering low noise, a high-frequency rate (1 kHz), and compatibility with a high-bias voltage source, making it more versatile than the MESON setup. The current-meter was paired with a Keithley 2400 SourceMeter to supply an arbitrary voltage.
Due to the periodic nature of the UCN signal, the wires were adjusted at specific moments to capture signals in both direct and reverse directions. After the scans, data are saved in xml and csv files so that they can be analyzed using Python scripts.

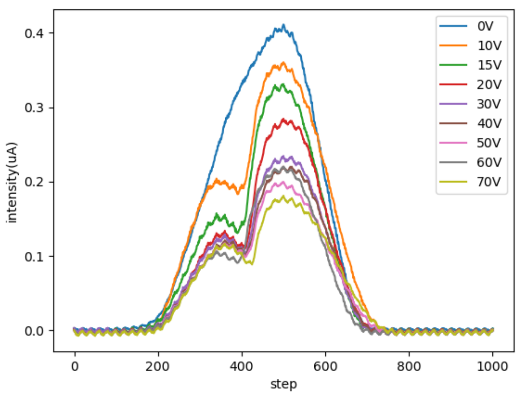

(A) horizontal wire (carbon nanotube)

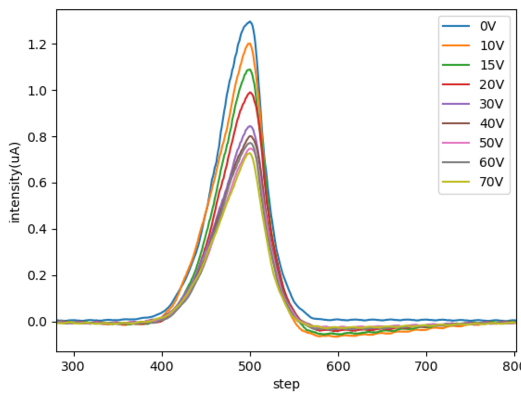

(B) vertical wire (Molybdenum)

FIGURE 4.1
Beam profiles from the horizontal and vertical wires for different bias voltages applied at both wires

The beam profiles of the wire in UCN, in Figure 4.1, show that as the bias voltage increases, the measured wire current decreases, ultimately stabilizing at a constant intensity level. This indicates that only a portion of the secondary electrons is recaptured by the wire.
Moreover, we observe a dip in the signal in each direction. When both signals are plotted together in

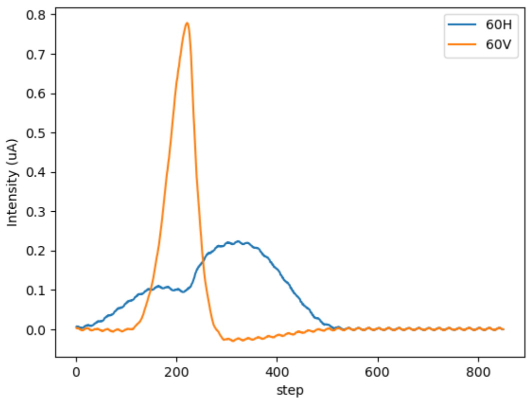

FIGURE 4.2
Beam profiles from the horizontal and vertical wires for a 60V bias applied at both wires

Figure 4.2, we can see that this decrease occurs when the other wire emits electrons. This dip in the signal is due to the electrons emitted from the other wire and captured by the wire under observation, which disturbs our transverse profile measurement.

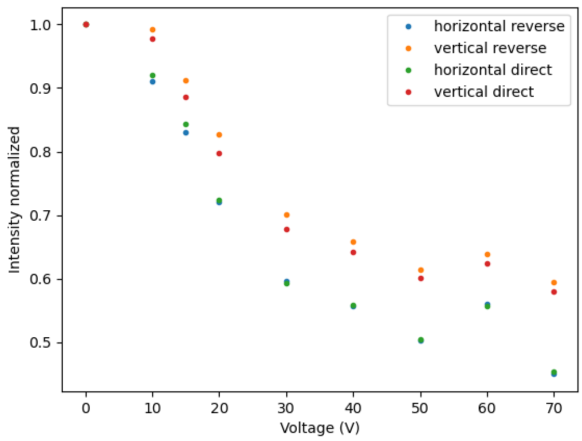

FIGURE 4.3
Intensity normalized to the 0V configuration for different bias voltages applied at both wires on UCN measurement

To reconstruct the profile without interaction we have considered that the signal is: $S_1 = S_{1,e} - S_{1,1} - S_{2,1}$, ie the sum of electrons that are escaping from wire 1, electrons that are coming back from wire 1 and electrons that were escaping from wire 2 and captured by wire 1. Considering that the signal on the wire at a given potential is a linear combination of signals on the wires without bias ($S_1 = \alpha_1 \cdot S_1(V = 0V) + \beta_1 \cdot S_2(V = 0V)$), we can reconstruct the signal without interaction between wires. Then, we can have the same plots as for RRL.In Figure 4.3, we observe that the signal tends toward a non-zero value, but the levels differ in both directions. This seems that there are changes in the configurations that enable us to distinguish the differences as the material or the radius of the wire or the beam shape.

Nevertheless, this plot is not telling all the story about low energy secondary electrons because a part of

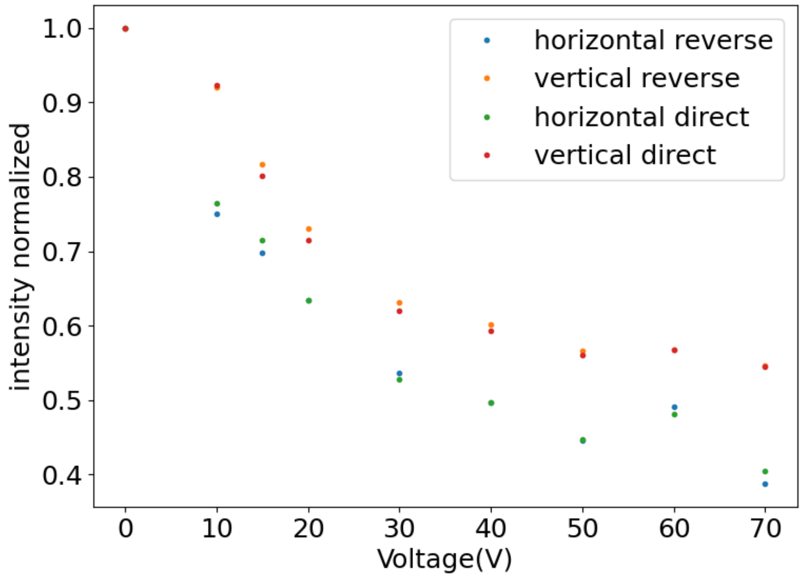

FIGURE 4.4
Intensity normalized to the 0V configuration for different bias voltages applied to both wires in the UCN measurement, with electrons emitted from one wire and detected on the other wire counted as signal for the first wire

them is captured by the other wire and not taken into account to quantify the secondary emission. In the Figure 4.4, we have used the same method but also considering electrons captured by the other wire but emitted by this one as part of the signal. We observe a lower signal especially for carbon nanotube wire decrease at last point of around 8%.

On top of that, we compared the results with measurements in the RRL. The wire is, first, placed at a given position in the ring, where we measure the intensity for different bias voltages. For this setup, we changed the connection to use the Keithley source-meter exclusively as a voltage source and current meter. This configuration limits the measurement to one wire at a time but allows automation with LabView scripts using a GPIB cable. The measurements can be completed automatically, saving beam intensity in one minute for analysis. We used wire 1 for the study and after the measurement, we made a profile measurement to observe the wire position on the beam for further analysis.

From Figure 4.5, we observe similar behavior to the cross wire, but with an additional dependence on recapture, which varies with the beam potential. This will be the focus of the next chapter. Furthermore, when we normalize the beam intensity by the value at zero bias, as shown in Figure 4.6, we find that all intensities converge to approximately 60% of the initial intensity. This indicates that this proportion is independent of the beam intensity but dependent on wire properties. This behavior tends us to reconsider delta emission proportion.

In general in a wire scanner, the impact of δ emission is considered as negligible compared to secondary electrons. Nevertheless, the measurements we have made suggest that δ emission is around the same

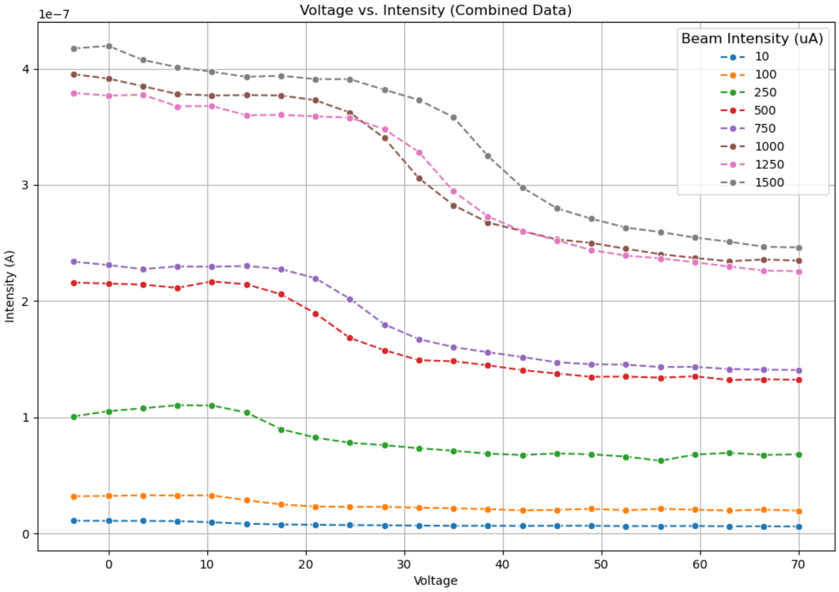

FIGURE 4.5
Intensity on the wire on the same position on the RRL at 502 MeV for different bias voltage and for different beam intensity(in μA) with their errorbar

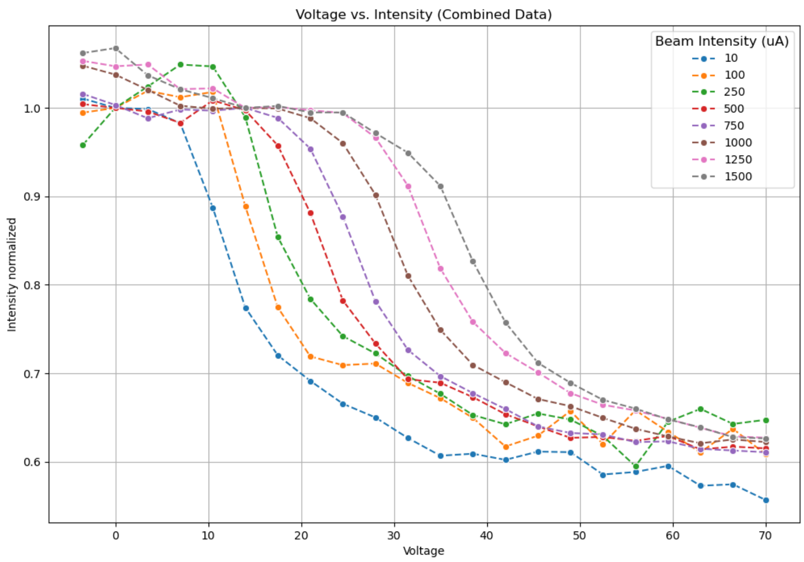

FIGURE 4.6
Intensity normalized to the 0V configuration for different bias voltages and different beam intensities on the same position on the RRL

fraction of emission of roughly 50%. This point suggests that the fraction of intensity will not really depend on the beam shape and position on the wire but more on the wire diameter, wire material and to a certain extent the beam energy.

4.2 SIMULATION/NUMERICAL COMPUTATION

In the absence of thermionic emission, electron emission occurs primarily through secondary and delta emission processes. To compute the total signal, it is necessary to carefully analyze both types of emission in detail.
For secondary emission, the Secondary Electron Yield can be calculated to quantify the signal obtained by the proton beam assuming the protons pass through two surfaces. However, the actual yield depends not only on the material but also on the surface quality and surface treatment. For example, prolonged exposure to radiation can degrade the surface, reducing the SEY due to changes in surface structure and electron binding properties.[28]
For δ emission, the computation is complex because of multiple scattering and the use of a particle transport code is necessary. The results were obtained using Geant4 version 11.2 with the G4EMStandardPhysics_option4 physics list using Monte Carlo method[18]. Then, for the correct material density, wire parameters, and beam energy, we can compute the electron emission probability by a proton.

The SEY and emission probability were reported in a previous article [29], and it can be concluded that these two quantities are comparable. The Table 4.1 summarizes the results for our configurations:

Material	Energy(MeV)	SEY contribution	Diameter (μm)	location
Carbon fiber	72	36%	33	RRL
Carbon fiber	590	37%	33	RRL
Molybdenum	590	59%	25	UCN
Carbon nanotube	590	77%	40	UCN

TABLE 4.1
Theoretical Secondary emission yield (SEY) contribution to the total electric current emitted for different wire configuration

We observe that high-density materials give a higher contribution from secondary emission to the signal.

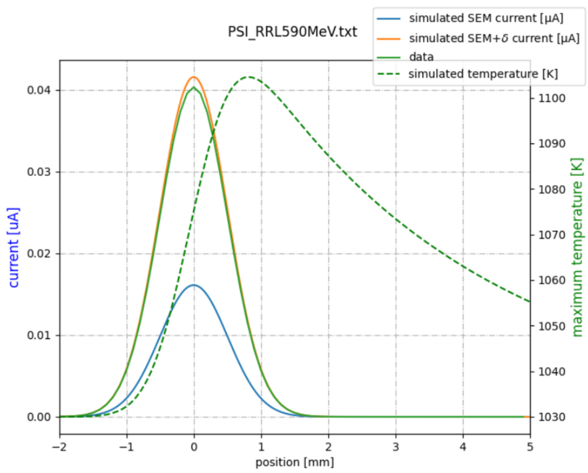

FIGURE 4.7
Simulation and comparison with data of intensity on the wire if we take into account δ-electron or not (Courtesy of Mariusz Sapinski)

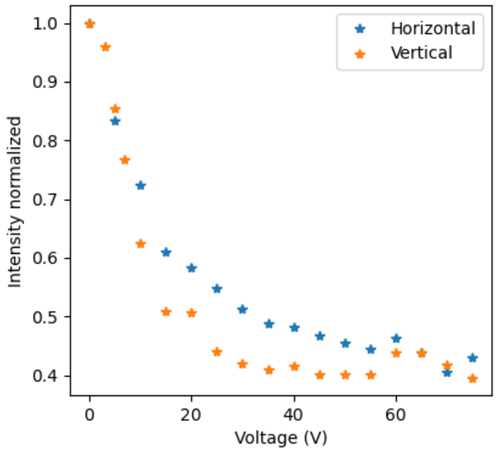

FIGURE 4.8
Normalized Intensity at different bias voltage for two molybdenum wires bias of 25μm at 1.5mA and 590MeV near SINQ (scanner MHP4546).

Moreover, if we simulate the signal received compared to data profile measurement, we observe from the figure that the contribution of secondary and δ emission is necessary to reconstruct the signal. Indeed, if we consider only secondary emission, we have only 40% of the signal, but with also delta-emission, the simulated signal converges to the data.
Now, we can compare our measurements with the theoretical SEY contribution. For the carbon wire, we obtain a contribution of approximately 40%, which is in good agreement with the theoretical value. For the Molybdenum wire, we measure a contribution of roughly 45% which is lower than expected. Similar measurements were made in a different place near SINQ with a in-shield wire in molybdenum.

In Figure 4.8, we observe that both molybdenum wires tend to 40 % of the initial intensity. So, we obtain for those two wires, a contribution of approximately 60% , which is in good agreement with the theoretical value.
The difference for the previous molybdenum wire could be the result of the degradation of the surface for those wires. Indeed, RRL wires are changed quite often, meanwhile UCN wires' last change was made a few months ago. Moreover, it could also be due to some external electromagnetic field that trap or make easier to recapture secondary electrons.
It suggests that we could recapture all low energy electrons emitted without really disturbing the signal because we could keep half the signal.

4.3 LIMITS ON BIAS VOLTAGE

The effect of the bias voltage, in the context of wire scanners, is to recapture electrons emitted by the wire. Nevertheless, in the presence of other sources of electrons, it can also capture those electrons.
Indeed, we have already seen in Figure 4.2 that in the presence of bias part of the electrons which are emitted by one wire are recaptured by the other wire. This phenomenon disappears when the wire isn't biased as we observe in Figure 4.1.

In the presence of multiple sources, the signal profile becomes significantly deformed in various ways,

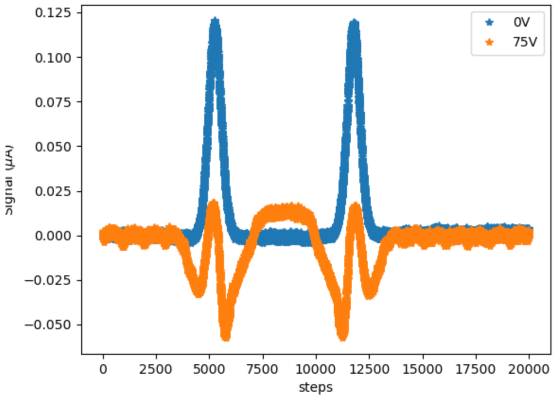

FIGURE 4.9
Vertical profile measurement In/Out of the beam with and without bias at 1.5mA near production target (scanner MHP4546).

as shown in Figure 4.9. First, we observe a decrease in peak intensity due to the recapture of secondary electrons. Then, at 6000 steps for the IN configuration and at 11500 steps for the OUT configuration, a dip appears in the profile, corresponding to the positioning of the horizontal wire. Finally, there is an observable offset modulation in specific segments: from 4000–7000 steps at -0.025 μA, from 7500–9500 steps at +0.015 μA, and from 10000–13500 steps again at -0.025 μA. This offset modulation appears even for 3V with similar amplitude. The offset is attributed to the varying recapture of electrons from the neutron production target near the profile monitor, which fluctuates depending on position during movement. These complexities make it challenging to accurately obtain the profile of the beam.

Chapter 5

Impact of the beam in the recapture

5.1 Beam impact on the applied voltage to recapture secondary electrons:experiment

In our previous experiment with the RRL, we observed that the beam intensity significantly influences the recapture of electrons by the wire. Specifically, as the beam intensity increases, a higher bias voltage is required to recapture all the low-energy electrons. This relationship is critical to understand the interaction between the beam and the wire's electron dynamics.
Further analysis suggests that if we exclude the initial slope observed at higher beam intensities ($\gtrsim 750$

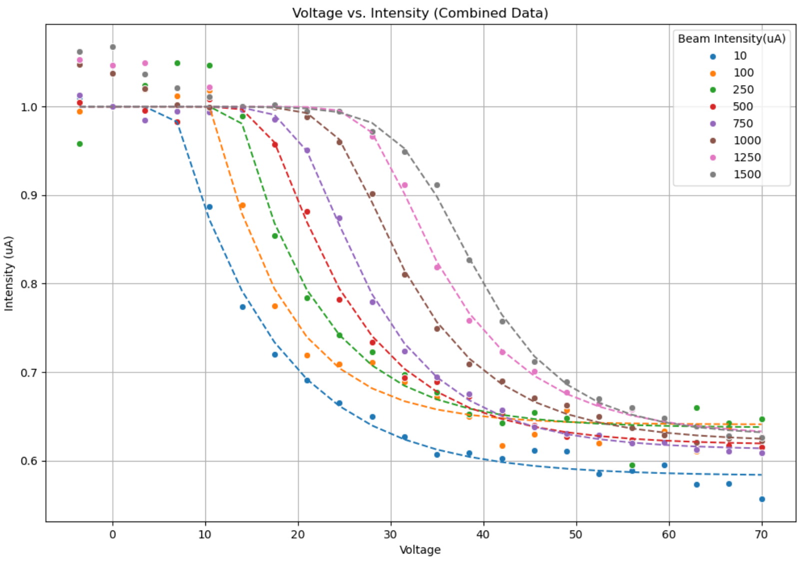

Figure 5.1
Intensity normalized to the 0V configuration for different bias voltages and different beam intensities on the same position on the RRL with the fit function not considering the first small slope

μA) where thermionic emission becomes noticeable, the curve can be accurately modeled by a sigmoid function:

$$I(V) = \frac{1 - I_\infty}{(1 + e^{\alpha(V - V_0)})^\beta} + I_\infty \tag{5.1}$$

In Figure 5.1, we can see that the fitting function closely matches our data, providing an excellent approximation of the observed behavior. This model allows us to explore the underlying physical processes more deeply, particularly the effect of the beam on the wire, through the analysis of the voltage required to halve the final intensity, as well as by comparing this value with the wire's intensity. The following figures (Figure 5.2) provide further insights into this analysis.

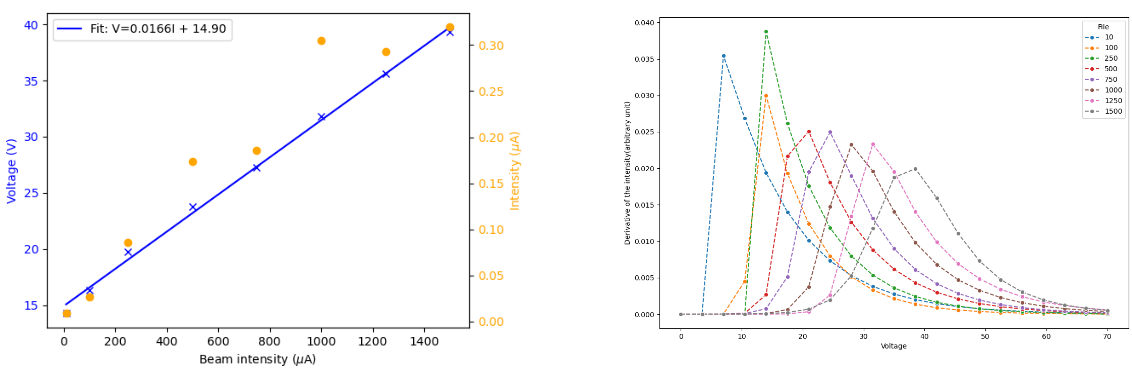

(A) Voltage Required to Halve Final Intensity for Varying Beam Intensities compared to Wire Intensity at this voltage

(B) Derivative of the intensity using the sigmoid fit function for different beam intensities: assimilated as a spectra of the secondary electrons

FIGURE 5.2

The data plotted in Figure 5.2a clearly show a linear relationship between the required voltage to halve final wire current and the beam intensity. This trend confirms the expected behavior, wherein a higher beam intensity necessitates a higher bias voltage to achieve the same electron recapture. This linear relationship is particularly useful for further analysis because it seems to be less susceptible to confounding factors than the wire intensity. Indeed, the wire current, while informative, is influenced by the beam's position relative to the wire, making it more difficult to isolate the beam's direct effect on the system.

Moreover, examining the derivative of the sigmoid function (Figure 5.2b) allows us to interpret these measurements as a secondary electron spectrum, providing deeper insight into the nature of electron recapture and the overall efficiency of the wire under varying beam intensities. This approach enables a more comprehensive understanding of the underlying physical processes governing electron dynamics in the presence of an external beam. We noticed a shift of the spectrum to higher voltages as the beam intensity increases, along with spectral broadening.

This dependence on the beam intensity suggests that there is also an impact of the electric field of the beam on the recapture of electrons by the wire. Indeed, with these intensities, the electric field and the beam potential start to be considerable compared to the wire potential and could do, for example, electron trapping.[30]
If we consider a 3D Gaussian beam, we can obtain the potential in the lab frame using this formula:

$$\Phi(x, y, t) = \frac{Q}{4\pi\varepsilon_0}\sqrt{\frac{2}{\pi}} \int_0^\infty \frac{e^{-\frac{x^2\lambda^2}{2(\lambda^2\sigma_x^2+1)} - \frac{y^2\lambda^2}{2(\lambda^2\sigma_y^2+1)} - \frac{(z-vt)^2\lambda^2}{2(\lambda^2\sigma_z^2+\gamma^{-2})}}}{\sqrt{\lambda^2\sigma_x^2+1}\sqrt{\lambda^2\sigma_y^2+1}\sqrt{\lambda^2\sigma_z^2+\gamma^{-2}}} d\lambda \tag{5.2}$$

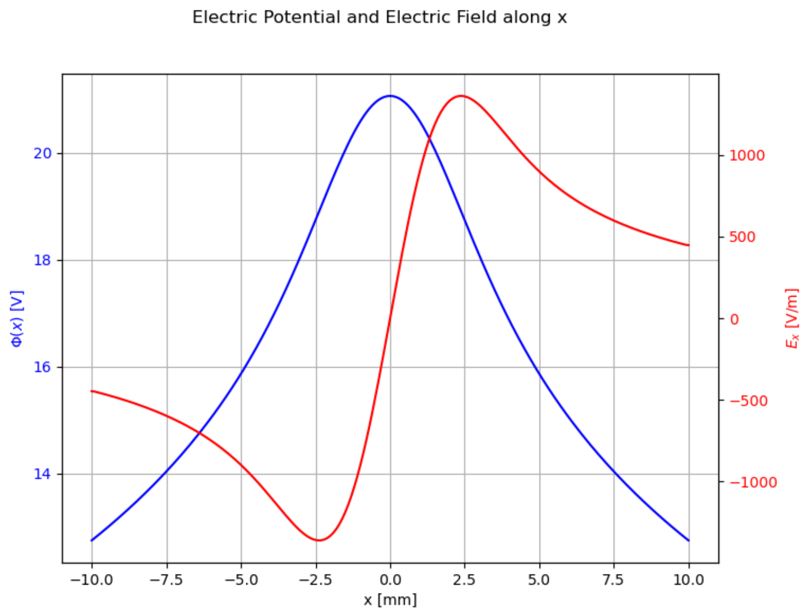

FIGURE 5.3
Potential and x-component of the Electric field in the lab frame along the x-axis generated by a beam of 1.5 mA with transverse size of $\sigma_{x,y}$=1.5 mm and σ_t=0.2ns from theory

where: Q is the charge of the beam,Φ the electrical potential.

Figure 5.3 shows that the maximum potential and electric field at the center of the bunch for a 590 MeV proton beam are 21 V and 1500 V/m, respectively. These values are on the same order as the wire bias. However, the potential seems too low to significantly impact the secondary electrons at 40 V. Furthermore, for UCN wires, we observe a lower impact on recapture; at 30 V, electrons are mostly recaptured for a 2 mA beam. This suggests that we should consider neighboring orbits spaced less than 1 cm apart for the 590 MeV proton beam.

We observed that with several neighboring orbits, as shown in Figure 5.4, the potential becomes significantly higher (66 V), which could have a more substantial impact on the beam.
Indeed, measurements of the profile beam in the cyclotron for all the orbits for different bias voltages were made using a battery as a voltage source. Then, we have done a ratio along the beam with the 0V bias profile.

In Figure 5.5, we observe that the signal is normalized along the beam to approximately 60%. Focusing on the 30 V curve, the ratio initially increases linearly to 1 at larger radii (corresponding to the first orbits) but decreases again as the radius becomes smaller. This trend highlights that the beam potential in the cyclotron depends on the spacing of neighboring orbits. At higher radii, the orbits are closer together, leading to stronger interactions. However, near the end of the trajectory at higher radii, the orbits predominantly converge in one direction, reducing the influence of neighbors and consequently lowering the potential.
Indeed, if we look into a lower radius in the cyclotron (5.6), we don't observe the plateau and the recapture of thermionic and secondary electrons seems to happens at 0V with no impact of the beam.
So it really seems that the beam impact is dependent of the spacing of neighboring orbits and we can't simulate rightly the situation without taking into account few orbits.

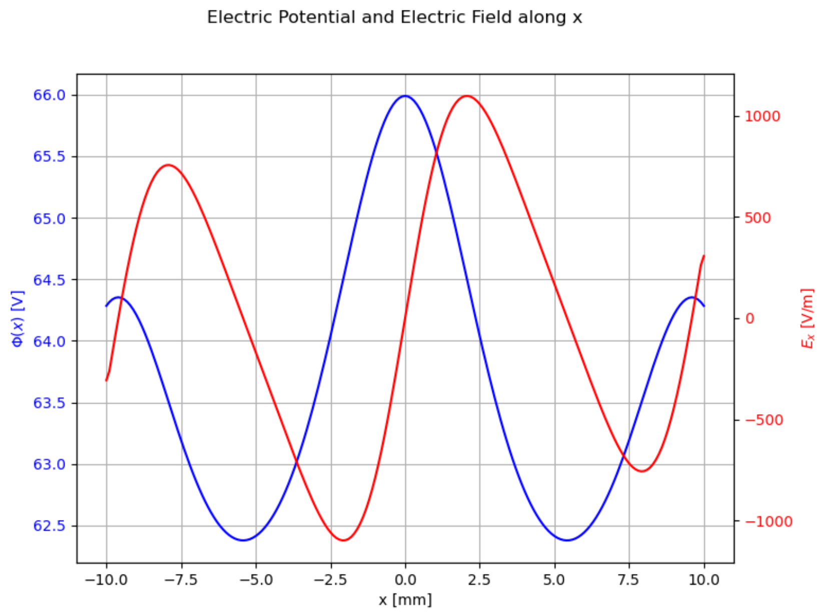

FIGURE 5.4
Potential and x-component of the Electric field along the x-axis generated by a beam of 1.5mA with transverse size of $\sigma_{x,y}$=1.5 mm and σ_t=0.2ns from theory and 2 orbits in both side spaced of 1 cm

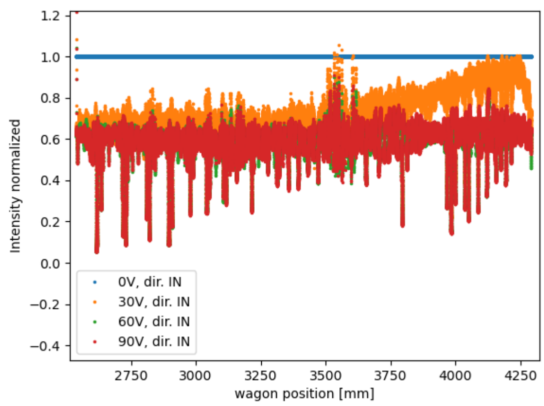

FIGURE 5.5
Profile measurement normalized to the 0V bias for wire 3 at 1.5mA for different voltage bias

Using Virtual-IPM[31], a software designed for simulating electron/ion transport, we initially examined the behavior of electrons in these configurations. However, it appears that the electric field generated by the proton beam was not strong enough to trap the electrons, allowing them to be recaptured by the wire. Nonetheless, we did not account for the longitudinal electric field, which, at these energies, could be non-negligible and may play a role in electron trapping.

Moreover, when we begin simulating the beam's interaction with the wire in CST using particle tracking and PIC (Particle-In Cell) solver [32], we observe that the electric field behaves differently.
Indeed, the figure 5.7a shows us the electric field along the x axis with no bias on the wire in the presence of the bunch. We observe at first the beam electric field comparable to the one plotted in Figure 5.3, but also, a much higher signal comparable to the signal of an electric field of a given potential.

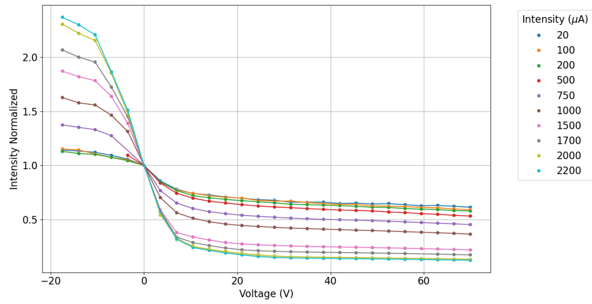

FIGURE 5.6
Profile measurement normalized to the 0V bias for wire 2 at 2.2m radius for different voltage bias and different beam energy

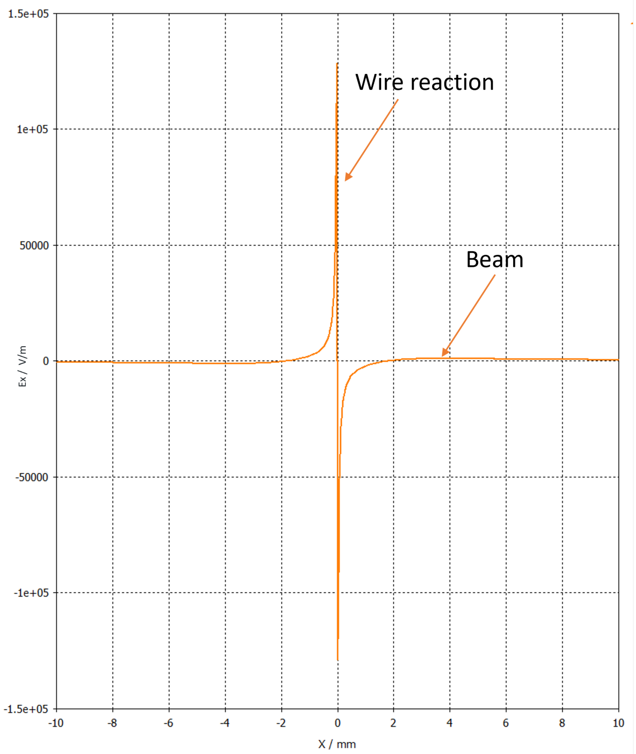

(A) Simulation on CST of the x-component of the Electric field along the x-axis in the presence of a carbon wire of 30 μm diameter and a proton beam with the same parameters as before.

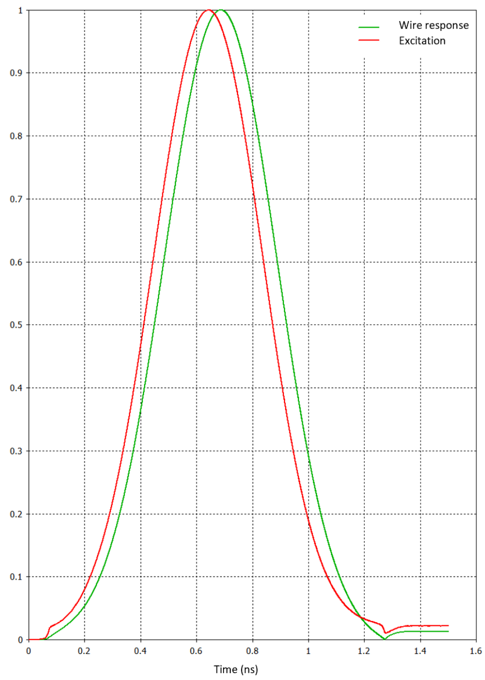

(B) Response of the wire electric field for an excitation of the proton beam of 590 MeV in arbitrary units.

FIGURE 5.7

It appears that the wire adjusts to the beam's potential by generating an external electric field to maintain its own potential. This electric field acts to repel electrons away from the wire. In the absence of an applied bias, the system can be viewed as a ring-shaped potential well. Additionally, the response time of the wire plotted in Figure 5.7b, based on the parameters I have implemented, appears to be relatively fast with a delay of 25 ps.

On Virtual-IPM, it's normally not possible to compute the interaction between the electric field and a wire. However, using a Python script, I was able to simulate this phenomenon by assuming that the wire's response is equal to the beam potential, with no delay, by tracking small time steps and adjusting the wire

bias at each step.
We then tracked the 5 eV electrons emitted transversely by the wire and observed whether they returned or not to the wire 15 ns after the beam interaction. At 590 MeV, with only the central orbit considered, every electron was coming back to the wire at 30 V.

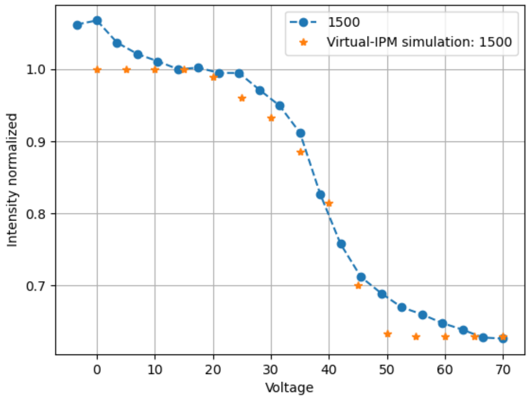

FIGURE 5.8
Comparison of the intensity normalized on RRL and simulation from Virtual-IPM for different voltages at 1.5mA at 590 MeV and with a 1.5 mm transverse size and one neighbor on both sides.

However, if we were considering the first neighboring orbit spaced of 1 cm, the results are different. For simplicity of comparison with the measured signal, we calculated the escape rate of electrons at each time step following their emission. Assuming the longitudinal shape as Gaussian with a size of 200 ps, we can have access to the fraction of secondary electrons escaping in the RRL configuration. Finally, I have converted this value to the intensity normalized considering δ-emission.
Upon comparing the experimental measurements with the simulation results from Virtual-IPM, as shown in Figure 5.8, we observe a general similarity in both the shape of the curve and the voltage at which the maximum slope occurs. Specifically, both the experimental data and the simulation show a similar trend in how the intensity changes with increasing bias voltage, with a sharp decrease followed by a plateau. The point at which the slope is steepest(indicative of the most significant change in intensity) appears at roughly the same voltage in both cases.
The simulation appears to correlate well with the experimental measurements; however, it relies on several approximations that may affect its accuracy. These approximations, such as idealized assumptions about the wire's behavior or the electron dynamics, should be carefully evaluated and verified to ensure that the model accurately reflects the underlying physical processes. While the general agreement between the simulation and the measurements is promising, further validation and refinement of the simulation would be necessary to improve its precision and reliability.
Moreover, simulations using CST were conducted to model a 590 MeV proton beam at 1.5 mA, including four neighboring orbits on each side. The setup consisted of a 30 V biased wire with a diameter of 30 μm and a length of 8 cm, as well as electrons with energies ranging from 2.5 to 7.5 eV.

In Figure 5.9a, we observe a slight decrease over time in the proportion of electrons that are not recaptured. After 20 ns (distance between bunches), 60% of the signal remains unrecaptured, even with a 30 V biased wire. Additionally, we notice that in figure 5.9b this ratio is influenced by the initial energy of the electrons. However, even for electrons with an energy of 2.5 eV, the uncaptured ratio is approximately 40%.
In the tracking of 5 eV electrons, shown in Figure 5.10, we notice that in the presence of the beam, the

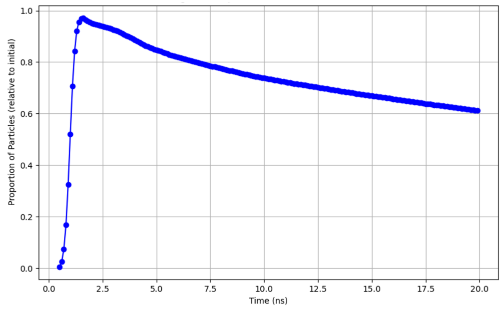

(A) Electron Escape Proportion in the Presence of a 590 MeV Beam with a 30V bias wire over Time from a CST Simulation

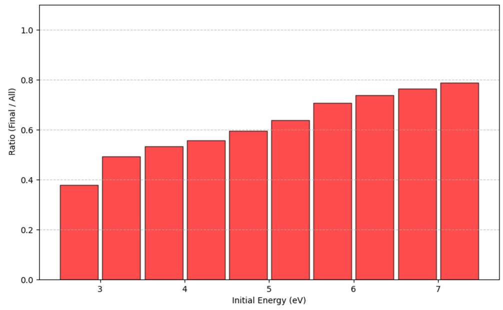

(B) Histogram of the ratio of electrons escaping in the Presence of a 590 MeV Beam for different energies from a CST simulation

FIGURE 5.9

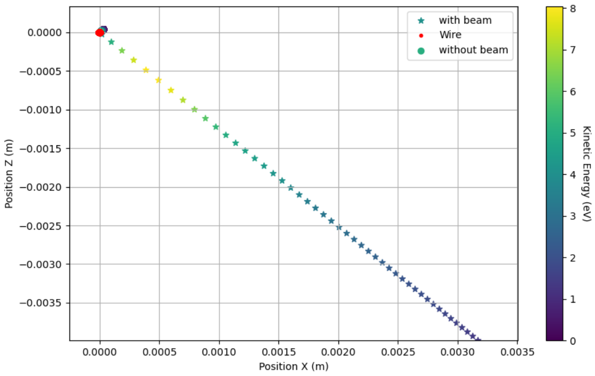

(A) Tracking of 5 eV electrons emitted by a 30 V biased wire with and without a 590 MeV beam at 1.5 mA from a CST simulation

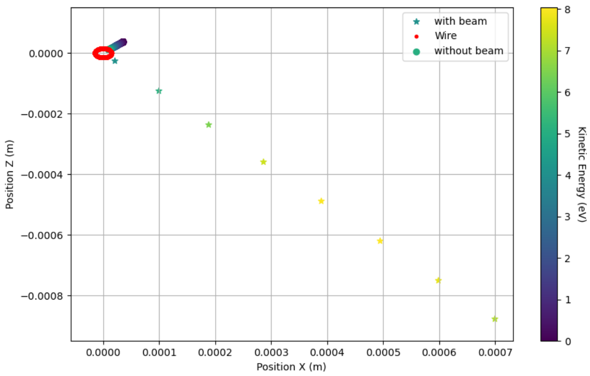

(B) Zoom on the tracking of 5 eV electrons emitted by a 30 V biased wire with and without a 590 MeV beam at 1.5 mA from a CST simulation

FIGURE 5.10

electron moves several millimeters away from the wire, compared to only a few tens of micrometers without the beam which is also observable in Virtual-IPM. Additionally, when observing the kinetic energy of the electron during the tracking, we see that it gains up to 3 eV of kinetic energy. This increase is not possible without the influence of the beam.

The simulations reveal that the beam's impact on the recapture process arises from an interaction between the charges in the wire and the beam's electric field. During the beam's passage, the charges within the wire redistribute to neutralize the electric field inside it. This redistribution generates a strong electric field outside the wire, which in turn repels the electrons emitted from the wire. Further analysis and simulations are needed to align the measurements with the simulations and better understand the underlying physics and key parameters driving this phenomenon.

CHAPTER 6

THERMIONIC EMISSION

In the previous sections, we focused on signals with little or no thermionic emission in order to observe the behavior of secondary electron emission and the impact of the applied bias and beam. However, it is important to recognize that the bias voltage is also influenced by thermionic emission, so it is crucial to examine its behavior more closely.
In earlier RRL measurements, we observed clear manifestations of thermionic emission. Specifically, at high beam intensities, two distinct slopes were evident: one at higher voltages (>30V) and another at lower voltages (<10V). The second one was previously neglected in our simulations and fittings. The lower-voltage slope would correspond to the recapture of most of thermionic electrons. Unlike secondary electrons, which are emitted only during the passage of the beam, thermionic electrons are emitted continuously from the wire. As a result, most thermionic electrons are not affected by the beam potential and are recaptured at lower bias voltages.

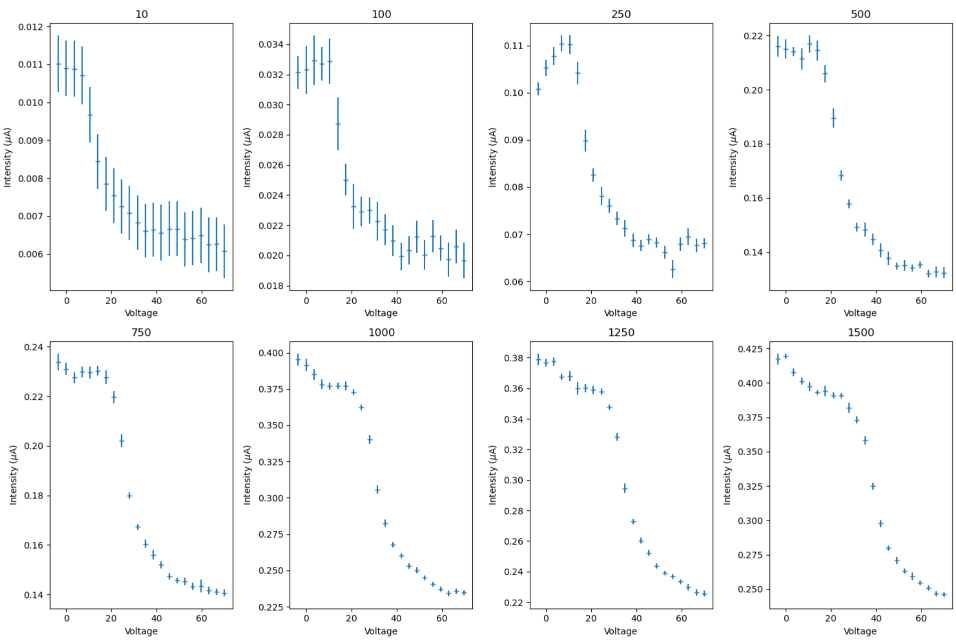

FIGURE 6.1
Intensity on the wire on the same position on the RRL for different bias voltage and beam intensities (in μA) at 502 MeV, including error bars(The uncertainties were calculated based on the manufacturer's information[33] and statistical analysis of 30 measurements for each data point)

A portion of the thermionic emission occurring during the beam's passage was previously neglected, as we assumed it to be relatively low during that time. However, this emission becomes more significant in cases with higher thermionic emission, where the effects can be observed more clearly.
We have repeated the measurements in positions where the wire was experiencing high thermionic emission. In Figure 6.2, we observe that, with this normalization, the three configurations converge to

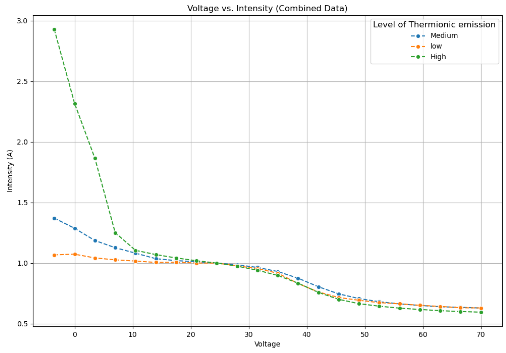

FIGURE 6.2
Intensity normalized at 21V on the wire on similar position for high/medium and low thermionic emission around 500 MeV on the RRL for different bias voltage at 1.5mA

the same value at around 60%. However, there is a significant decrease in intensity corresponding to thermionic electrons recaptured by the wire for low bias. We observe that contrary to the idea, we need

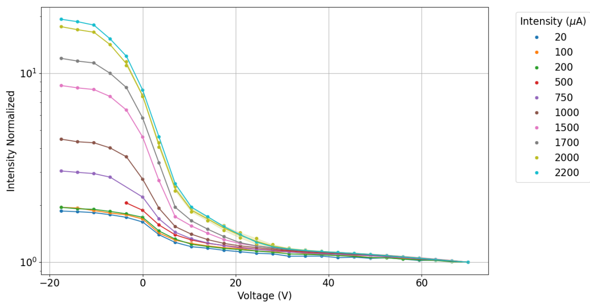

FIGURE 6.3
Intensity normalized and shifted to subtract the dependence of secondary emission (subtract the curve of 20μA) from the same data as Figure 5.6

more than 10 V to recapture thermionic emission. The first conclusion was that this was due to the beam impact but new studies highlights in Figure 6.3, highlights that this behavior could be intrinsic to the thermionic recapture.
Contrary to the previous studies, it suggests also that possibly all thermionic emission could be recaptured by bias voltage. To support this hypothesis, I wanted to compare it with the previous data (from 2022) because it also allows me to have an all scan and not only at a given position and at different energies.
The measurement was made by adding batteries in a series with the Meson and obtaining the data. Then, I have compared the scan for different biases (0V/30V/60V/90V) and observed the ratio between the 0V and the different biases.

In Figure 6.4a, we observe a significant decrease in thermionic emission with the application of bias voltage, demonstrating the strong suppressive effect of the bias on thermionic processes. Additionally, Figure 6.4b shows that the ratio near the thermionic emission stabilizes around 60%, which could suggest

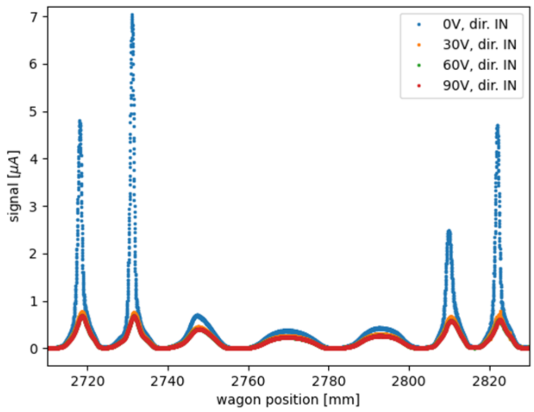

(A) Profile measurement at 1.5 mA for different bias voltage between 2710 mm and 2830 mm

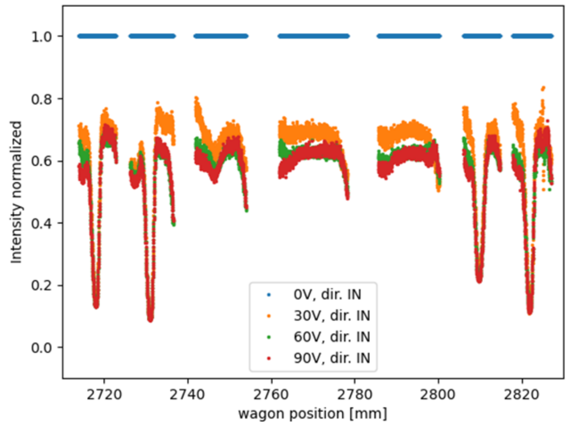

(B) Ratio of Profile measurement at 1.5 mA for different bias voltage between 2710 mm and 2830 mm

FIGURE 6.4

that thermionic emission is suppressed. However, the orbit profile at 90V indicates the presence of residual thermionic emission, as evidenced by a pronounced peak accompanied by a Gaussian-like beam in the tails, consistent with observations in [27]. This phenomenon could be attributed to a high initial current generating a narrow beam that, due to space charge effects and other interactions, creates a halo in the beam's tails. This explanation is further supported by the profiles at lower intensities, which appear sharper and more confined. To verify this hypothesis, we propose a method that involves summing the orbit intensities for various beam intensities and bias voltages, and subsequently plotting the resulting values as a function of beam intensity. At low intensities, the graph is expected to exhibit a linear relationship. In the absence of thermionic emission, this linearity would persist; however, the presence of a thermionic signal would manifest as a deviation, causing an increase in the data beyond the expected linear trend if we neglect the beam impact.

Figure 6.5a reveals two distinct behaviors in the data. At low beam intensities, a linear trend is evident, with the gradient decreasing gradually from $4,68.10^{-15}$ C$/\mu A$ to $2,90.10^{-15}$ C$/\mu A$, a reduction of 61.8%. This observation aligns well with theoretical predictions.In contrast, at higher beam intensities, the total charge exceeds the linear trend at low bias voltages due to thermionic emission. However, as the bias voltage increases, these data points also converge toward the linear curve, showing that the thermionic emission is totally recaptured at higher voltages.
Furthermore, comparing the beam profiles as a function of bias voltage for this orbit in Figure 6.5, we observe that, after rescaling the 1.5 mA beam to account for its higher intensity, the profiles for high and low beam intensities align well at high bias voltages (60 V), while at zero bias, the 1.5 mA beam exhibits significantly higher thermionic emission.
These new measurements suggest that all thermionic emission is recaptured by the biased wire, contrary to the conclusions of the previous study. To reconcile the earlier results with this new understanding, we propose that the beam profile's shape may be influenced by intensity, potentially consisting of both a narrow beam and an additional halo component.

Furthermore, secondary emission was analyzed using data from orbit 10, where the final ratio was found to be 67%, higher than initially expected. This discrepancy was also observed for wire 1 and appears to result from a residual magnetic field, which partially recaptures electrons in wire 1. This effect is negligible for other wires because the electron emission in those cases is not orthogonal to the beam field. Since this phenomenon depends on the wire's position, it could significantly impact the estimation of

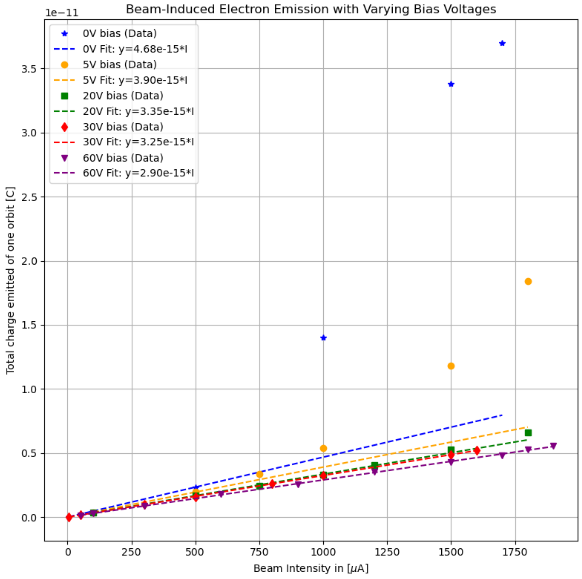

(A) Total Charge measured on the 16 orbit for different beam intensities and bias voltage with the linear for low intensity

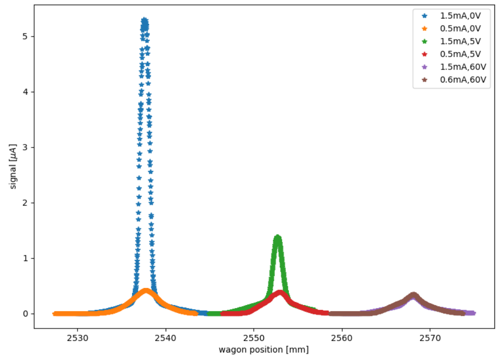

(B) Profile Measurement of orbit 16 (123MeV) on wire 2 for different voltages and at 1.5 mA and around 0.5mA (The 1.5mA profile is rescaled to fit the other profile)

FIGURE 6.5

secondary emission in specific cases.

Chapter 7

Conclusion and Perspectives

The wire scanner is a commonly used measurement tool in particle accelerator physics. However, the underlying physics is not well understood, and several aspects are still under discussion.
First, we observed that, contrary to previous studies, thermionic emission appears to be fully recaptured by the bias voltage. Furthermore, we demonstrated that, contrary to expectations, the δ emission is of the same order of magnitude as secondary electron emission. This suggests that we can maintain half of the signal while recapturing all thermionic emission under bias conditions, without canceling the signal entirely.
However, we also observed that the bias voltage could be much higher than anticipated due to the wire's reaction during beam passage, which alters the charge distribution in the wire and causes a repulsion of the emitted electrons. Future studies are needed to explore this effect further and to align the simulation results with experimental measurements.

While applying bias to suppress thermionic emission proves effective, the required bias is considerably larger than initially anticipated and varies with beam intensity. As discussed in Chapter 5, the wire bias may also recapture electrons from other sources, which could distort the measured signal. Additionally, since thermionic emission serves as a cooling mechanism, the recapture of electrons could negatively impact the wire's cooling efficiency. These factors highlight the complexity of the system and suggest the need for further optimization or a passive method.

To overcome these challenges, we propose a non-invasive technique for measuring the beam profile. This method takes advantage of the distinct frequency characteristics of secondary electron emission and thermionic emission. Thermionic emission typically manifests as a low-frequency signal because the cooling process is not fast enough between bunches, while secondary electron emission occurs at higher frequencies corresponding to the beam's bunching. By isolating the high-frequency component from the wire's signal, we can effectively eliminate the influence of thermionic emission and obtain a more accurate measurement. Although a first attempt was made to apply this method, it was unsuccessful, indicating the need for further refinement.

Bibliography

[1] *PSI in Brief*. PSI. URL: https://www.psi.ch/en/about/psi-in-brief (visited on 05/11/2024).

[2] *The PSI proton accelerator*. PSI. URL: https://www.psi.ch/en/research/the-psi-proton-accelerator (visited on 05/11/2024).

[3] *Ultra Cold Neutron Source*. PSI. URL: https://www.psi.ch/en/ucn (visited on 07/11/2024).

[4] *Injector 2: A pre-accelerator for protons*. PSI. URL: https://www.psi.ch/en/media/our-research/injector-2-a-pre-accelerator-for-protons (visited on 05/11/2024).

[5] M.Seidel J.Grillenberger C.Baumgarten. 'The High Intensity Proton Accelerator Facility'. In: *SciPost Physics Proceedings, no. 5, Sep. 2021*. DOI: 10.21468/scipostphysproc.5.002.

[6] *SμS:Swiss Muon Source*. PSI. URL: https://www.psi.ch/en/smus (visited on 07/11/2024).

[7] *Cockcroft-Walton*. PSI. URL: https://www.psi.ch/en/cas/cw (visited on 11/11/2024).

[8] B.Blau B.Lauss. 'UCN, the ultracold neutron source – neutrons for particle physics'. In: *https://doi.org/10.48550/arXiv.2104.02457*.

[9] *SINQ: The Swiss Spallation Neutron Source*. PSI. URL: https://www.psi.ch/en/sinq (visited on 07/11/2024).

[10] K.Wittenburg. 'Specific instrumentation and diagnostics for high-intensity hadron beams'. In: *CAS - CERN Accelerator School: Course on High Power Hadron Machines: 24 May - 2 Jun 2011, Bilbao, Spain*. DOI: 10.5170/CERN-2013-001.251.

[11] M.Sapinski. 'About the damage mechanisms of thin targets exposed to high-power particle beams'. In: *Proc. IPAC'23, Venice, Italy, May 2023*. DOI: 10.1088/1742-6596/2687/7/072016.

[12] J. Rumble. *CRC Handbook of Chemistry and Physics, 104th*. CRC Press, Ed, Boca Raton, Florida: Taylor Francis Group, 2023. ISBN: 9781032425207.

[13] M. Sapinski, R. Dölling and M. Rohrer. 'Commissioning of the renewed long radial probe in psi's ring cyclotron'. In: *Proc. IBIC'22, Kraków, Poland, Sept. 2022*. DOI: 10.18429/JACOW-IBIC2022-MOP19.

[14] R.Dölling, M. Sapinski and F. Marcellini. 'Test of a prototype for modular profile and position monitors in the shielding of the 590 MeV beam line at HIPA'. In: *Proc. IBIC'22, Kraków, Poland, Sept. 2022*. DOI: 10.18429/JACoW-IBIC2022-MOP24.

[15] R. Dölling. 'Progress with bunch-shape measurements at PSI's high-power cyclotrons and proton beam lines'. In: *Proceedings of HB2012, Beijing, China p187-189*.

[16] J. Bosser, J. Camas and L. Evanss et al. 'The Micron Wire Scanner at the SPS'. In: *Technical report at CERN, 1987*.

[17] F. Herbert Attix. *Introduction to Radiological Physics and Radiation Dosimetry*. Wiley, 1986. Chap. 8-Charged particle interactions in matter.

[18] J.Allison et al. 'Recent developments in Geant4'. In: *Nucl. Instr. Meth. A, vol. 835, p. 186-225, 2016*. DOI: https://doi.org/10.1016/j.nima.2016.06.125.

[19] E.J. Sternglass. ‘Theory of Secondary Electron Emission by High-Speed Ions’. In: *Physical Review, vol. 108, no. 1, pp. 1–12, Oct. 1957*. DOI: https://doi.org/10.1103/physrev.108.1.

[20] S. Seltzer. ‘Stopping-Power & Range Tables for Electrons, Protons, and Helium Ions’. In: *NIST Standard Reference Database 124, 1993*. DOI: https://dx.doi.org/10.18434/T4NC7P.

[21] A.Navarro. ‘Understanding Secondary Emission Processes and Beam Matter interactions for Optimization of Diagnostic Wire Grid System in Particle Accelerators’. PhD thesis. Universitat Politecnica de Catalunya, BarcelonaTech, Barcelona, 2016.

[22] D. Hasselkamp, S. Hippler and A. Scharmann. ‘Ion-induced secondary electron spectra from clean metal surfaces’. In: *Nuclear Instruments and Methods in Physics Research Section B: Beam Interactions with Materials and Atoms, vol. 18, no. 1-6, pp. 561–565, 1986*. DOI: https://doi.org/10.1016/s0168-583x(86)80088-x.

[23] M. S. Chung and T. E. Everhart. ‘Simple calculation of energy distribution of low-energy secondary electrons emitted from metals under electron bombardment’. In: *Journal of Applied Physics, vol. 45, no. 2, pp. 707–709, Feb. 1974*. DOI: https://doi.org/10.1063/1.1663306.

[24] W.B Nottingham. *Electron-Emission Gas Discharges I*. Encyclopedia of Physics / Handbuch der Physik, vol 4 / 21. Springer, Berlin, Heidelberg, 1956. Chap. Thermionic emission. DOI: https://doi.org/10.1007/978-3-642-45844-6_1.

[25] O. Richardson. *The Emission of Electricity from Hot Bodies*. Published by Longmans Green and Company, London. 1916.

[26] K. Uppireddi et al. ‘Thermionic emission energy distribution from nanocrystalline diamond films for direct thermal-electrical energy conversion applications’. In: *Journal of Applied Physics, vol. 106, no. 4, p. 043 716, Aug. 2009*. DOI: https://doi.org/10.1063/1.3204667.

[27] M.Boucard and M.Sapinski. ‘Dealing with thermionic emission in wire scanners based on secondary electron emission’. In: *Proc. IPAC’23, Venice, Italy, May 2023*. DOI: 10.18429/JACoW-IPAC2023-THPL150.

[28] G.Rumolo et al. ‘Electron Cloud Effects at the LHC and LHC Injectors’. In: *Proc. IPAC’17, Copenhagen, Denmark, May 2017,paper MOZA1, pp. 30–36*. DOI: https://doi.org/10.18429/JACoW-IPAC2017-MOZA1.

[29] M.Sapinski. ‘Secondary, thermionic and delta electron emission from thin targets’. In: *Proc. IBIC’24, Beijing, China, Sept. 2024*. DOI: n.b.

[30] M.Sapinski et al. ‘Application of machine learning for the IPM-based profile reconstruction’. In: *Proceedings of the 61st ICFA Advanced Beam Dynamics Workshop, Daejeon, Korea, June 2018*. DOI: 10.18429/JACoW-HB2018-THA2WE02.

[31] *Virtual-IPM*. URL: https://gitlab.com/IPMsim/Virtual-IPM.

[32] *CST*. URL: https://www.3ds.com/products/simulia/cst-studio-suite.

[33] *Datasheet of Keithley 2400 sourcemeter*. URL: https://download.tek.com/datasheet/1KW-2798-3_2400_SourceMeter_SMU_Datasheet_041121.pdf.